In situ scanning tunneling microscopy of organic self-assembled monolayers on HOPG

William Wenig[1], Yoshua Hempel[1], Nikolai Severin[1,2,3]

[1]Institut für Physik, Humboldt-Universität, 12489 Berlin, Germany
[2]IRIS Adlershof, Brook-Taylor-Straße 6, 12489 Berlin, Germany
[3]Supervision of lab course

In this advanced lab course we acquainted ourselves with the functionality of a scanning tunneling microscope and its utility to generate high-resolution gray scale images of different scanning ranges with highly pyrolytic graphite as the calibration material. We determined the unit cell dimensions of the self-assembled monolayers of arachidic acid molecules to be $a = 0.953(4)$ nm, $b = 3.06(5)$ nm with an angle of $82.21(4)^\circ$ between the unit cell vectors. We also characterized monolayers of hexa-peri-hexabenzocoronene molecules with $a = 2.90(2)$ nm, $b = 4.78(5)$ nm and an angle of $106.8(5)^\circ$. We utilized the Nanosurf NaioSTM at scanning ranges of 10 nm to 20 nm to also determine the intermolecular distance of the arachidic acid molecules in their monolayer to be $d_{mol} = 4.689(3)$ Å using a Moiré pattern. We related our investigation to other works in the field and understood the process of global image correction by utilizing affine and Fourir transformations.

With the invention of the scanning tunneling microscope (STM) in 1981 [1] and the following Nobel Prize in Physics in 1986, G. Binnig, H. Rohrer and coworkers introduced a new imaging technique to study structures on the atomic scale. The development of the last 40 years extended this approach in order to use the STM outside of this scope for assembling [2] and manipulating [3] single atoms of a surface, inducing and studying chemical reactions [4] and also generalizing the underlying principle to what is now the class of scanning *probe* microscopes [5]. The STM is responsible for major breakthroughs in nanotechnology and various other disciplines because it bears crucial advantages over other high-resolution electron-based imaging techniques. One such advantage is the ability to operate in various fluid ambients. This enables us to gather atomic-scale information of solid-fluid-interfaces like self-assembled monolayers of organic molecules [6]. The study of these monolayers is of major importance because their constituents are tunable regarding structural, electronic and chemical properties. This makes them promising candidates for the use in novel electronic and optoelectronic devices.

In this lab course we understood the working principle of an STM by investigating highly oriented pyrolytic graphite (HOPG) at ambient conditions and by performing structure characterizations on self-assembled monolayers of arachidic acid and hexa-peri-hexabenzocoronene (C_{12}-HBC) on top of HOPG in a fluid milieu. Figure 1 shows the structural formulas of these organic compounds.

1 Methodological details

In our experimental setup we utilized the commercial NaioSTM from Nanosurf. It comes with its own airflow shield and passive vibration isolation feet on a stone plate. The manufacturer claims that this setup will yield atomic resolution even in non-isolated environments. We were not able reproduce this behavior hence we set up the STM on a granite countertop with dimensions of (150x50x5) cm which hang on elastic ropes from the ceiling. We equipped the STM with

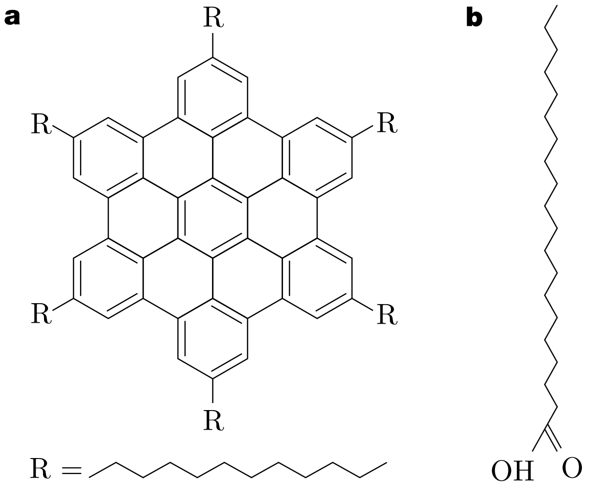

Figure 1 | Chemical structure formulas of the organic molecules used for investigating monolayers. a) Structure of a single hexabenzocoronene molecule substituted with alkyl side chains (R) which constitutes hexa–peri-hexabenzocoronene. **b)** Structure of arachidic acid ($C_{20}H_{40}O_2$) where the long carbon chain is connected to the carboxylic group that forms the head of the molecule.

alloy tips of 80% Platinum and 20% Indium and prepared them with a pair of wire cutters by truncating a PtIn-wire with a diameter of 0.25(3) mm. In order to produce sharp tips and ultimately increase resolution, we made an effort to cut the wire each time at an angle of 45°. Whilst avoiding collisions with any surface, the wire segments were put into the inset of the NaioSTM using pliers.

We induce the highly interfacial phase of the organic compounds shown in figure 1 by utilizing HOPG as a calibration material like in previous investigations [6]. HOPG exhibits a highly ordered, layered and unpolar structure which makes it a great candidate for this application. The inter-layer interactions in HOPG are only that of Van-der-Waals nature which permits us to cleave off layers with a piece of tape. This procedure leaves behind a fresh and clean surface, on which we performed our STM imaging. We operated our STM in constant height mode by shifting most of the contrast into our current-image rather than into our topography-image.

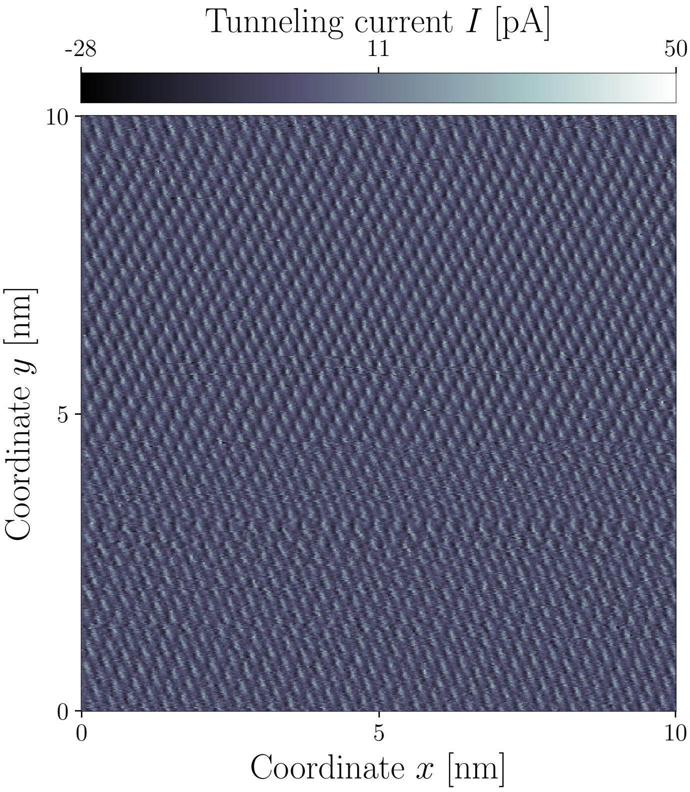

Figure 2 | The unprocessed output of a scanning tunneling microscope is subject to many distortions. Tunneling current I displayed in the controller reference frame (x, y) for the surface of HOPG at ambient conditions. The scanning range of 10 nm reveals a distorted but hexagonal structure of graphite with horizontal scars.

2 Data processing

Figure 2 illustrates one of the images we obtained from the STM for the bare surface of of our HOPG sample. All images showcase various artifacts. Alongside the noise caused by statistical factors, such as temperature and vibration, we can see horizontal scars in our images. These could have conceivably been caused by a sudden drift by the material or loss of tip interaction, as the tip itself changes its physical properties during the scanning procedure. Another distortion in the images is caused by a drift of the tip relative to the sample, which we are going to assume to be of constant velocity. The vertical component of the drift contributes as a linear change in the tunneling current, in this case increasing over time.

The drifts parallel to the plane of the sample result in a skewing and stretching of the image itself and can be described by a linear transformation of the desired image. In other words if the function $f(x, y)$ describes the actual structure of the crystal surfaces, the image we received is of the form $f' := f \circ A$. Here A describes a linear transformation in $\mathbb{R}^2$, which displaces the coordinates of the amplitudes from where they would have been measured without the drift. So if in an ideal measurement we would have measured an amplitude $f(x, y)$ at (x, y). In the real measure-

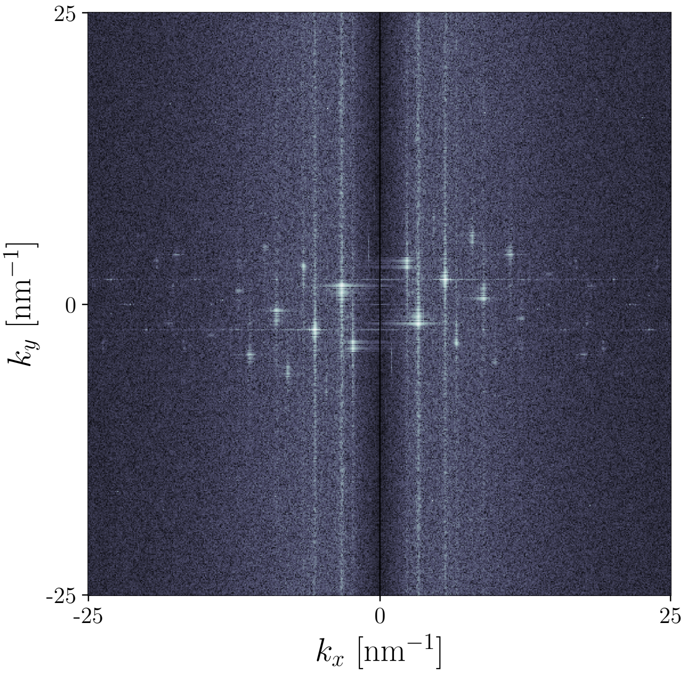

Figure 3 | Revealing stretches and other distortions of the unprocessed output in Fourier space. The FFT of the unprocessed output of the STM on a scanning range of 10 nm. It condenses the affine character of the distortion by deviating from the usually hexagonal structure of the reciprocal lattice of graphite.

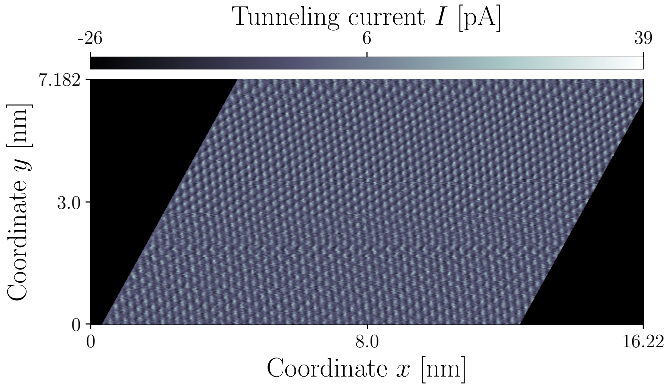

Figure 4 | Scarring and local skews still persist after the correction through an affine transformation. Tunneling current I displayed in the approximated sample's frame of reference (x', y') for HOPG at ambient conditions. The image correction was done through an affine transformation with SPIP. Distortions are still visible which suggests that this correction cannot capture local distortions.

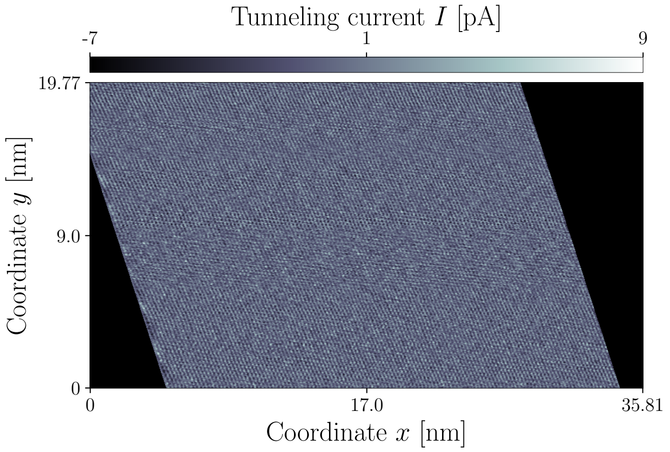

Figure 5 | Higher scanning ranges present the exceptional regularity of the graphite sample at the cost of resolution. Scan image of HOPG sample at ambient conditions with a scanning range of 20 nm. The image was transformed into the sample's frame of reference (x', y').

ment we measured $f(x', y')$ with $(x', y') = A^{-1}(x, y)$. However, since we know the crystal structure of HOPG, we can correct this distortion of the image by finding the linear transformation that restores its hexagonal structure and apply it to the whole image. In order to do this, we use the discrete Fourier transformation (FFT) of an image of HOPG, illustrated in figure 3.

In this FFT we find two neighboring lattice vectors of the reciprocal unit cell. Utilizing the SPIP software we then construct a linear transformation and map these lattice vectors onto the two lattice vectors of the undistorted unit cell of HOPG. This transformation has a degree of freedom in the orientation of the unit cell where as little rotation as possible in the image is desired. This is because rotations deviating from a multiple of 90° necessitate more interpolation between pixels. Apart from that there is also the choice of lattice vectors in the theoretical reciprocal lattice we want to map onto, which is chosen to be the closest ones to those selected in the input image. All of these choices are made automatically by SPIP. One way to eliminate the rotation in the transformation is by QR-decomposition of the matrix, although we don't know whether SPIP uses this specific method. Any real matrix A can be decomposed into an orthonormal part Q and an upper triangular part R. In our case we can assume the diagonal elements of R to be positive and we can find R by applying the Cholesky decomposition method to $A^T A = R^T Q^T Q R = R^T R$. Applying the matrix R obtained in this way will correct the drift without any rotation. This linear transformation can now be used to restore the crystal structure in the real space image as well. But we found that it is not possible to simply apply the same transformation we used for correcting the FFT. One way of solving this issue is to apply it to the FFT of the image we want to correct and then apply an inverse FFT, but this is running the risk of heavily falsifying the data, as it applies the inverse FFT to an image, which has interpolated pixels and skewed edges. We instead utilized the properties of the Fourier transform, also called the Affine theorem, with which an affine transformation in the image domain induces a corresponding transformation in the Fourier domain.

$$\mathcal{F}\big[f \circ M\big] = \big|\det M^{-1}\big| \cdot \mathcal{F}\left[f \circ \left(M^{-1}\right)^T\right]$$

$$\Leftrightarrow \mathcal{F}\left[f \circ \left(M^{-1}\right)^T\right] = \big|\det M\big| \cdot \mathcal{F}\big[f \circ M\big]$$

where M is a linear map in $\mathbb{R}^2$. This means, applying a linear map M to the Fourier space of an image is equivalent to applying $\left(M^{-1}\right)^T$ to the real space image and vice versa.

Comparing the unprocessed image of the HOPG surface in figure 2 to the result obtained in figure 4 via this post processing workflow, one can see that the expected crystal structure has been restored, albeit results vary across the image. In the center of the image the hexagonal structure is symmetrical to the eye, whereas it is still fairly skewed at the bottom. These two sections of differing veracity are separated by horizontal scars in the image, which suggests a sudden change in the relative velocity between sample and tip. This could be a problem, when trying to apply this correction to images containing samples other than HOPG, as even if the graphite crystal structure in those images is perfectly symmetrical, the other sections can

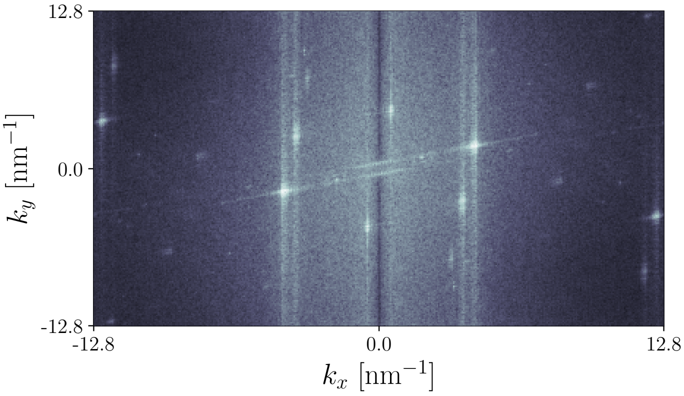

Figure 6 | A higher scanning range improves the resolution of image in Fourier space yet worsens the signal-to-noise ratio. FFT of the unprocessed output at a scanning range of 20 nm. The artifacts of the lower resolution of the crystal structure in the unprocessed image render into a glow in Fourier space.

still be considerably distorted. The corrected FFT still appears to be stretched along the x-axis. This is due to the dimensions of the image changing, since the unit of the argument of the discrete Fourier transform along a given axis has an inverse relationship to the number of elements, or in this case pixels, contained in it. We also captured images of our HOPG sample at a scanning range of 20 nm. We illustrate the processed image in figure 5. The details of the crystal structure are significantly worse resolved in the real space. But the resolution of the FFT's unit cell seen in figure 6 is improved compared to the one of the images with a scanning range of 10 nm. That could result in a reduction of error in the affine transformation, as the reciprocal lattice vectors can be located more accurately in the FFT. The accuracy of the method of correction by affine transformation is limited by several factors. The most glaring issue is the assumption within that the distortion is uniform across the image, which as we've seen with this example is not always a good one. There are several reasons for why this might happen, but to understand why, one must first look at the reasons for what causes the distortions in the first place. Several causes of drift and ways to account for them are described in the work of Yothers et al. [7]. One of the described causes are fluctuations in temperature both dependent on time and space. The distance between tip and sample is highly influenced by such changes as it is typically 3 to 4 orders of magnitude smaller, than the scanning range width. If there is a constant temperature gradient throughout the image, its effect can be described as a shearing and stretching of the image, which can be corrected using the affine transformation method [7].

Another cause of distortions lies within properties of how piezoelectric actuators operate in practice, as they are subject to piezoelectric actuator hysteresis and actuator creep [7]. Because of the hysteresis the voltage-position curve of the actuators changes depending on their history. The effect of this on the image is a stretching of the image in x-direction at the beginning of each scan line, which decreases along the x-axis in scanning direction, making it an intrinsically non-uniform effect. Piezoelectric actuator creep describes the way in which they approach the position at which the bias potential is measured. There will always be an offset between the equilibrium position, the crystal is moving towards and its own. The position will then get closer logarithmically. In other words, if for a fixed voltage the position of the actuator at a time t is $l(t)$, then after an initial dynamic motion towards the equilibrium, it will be of the form [8]

$$l(t) = l(t_0)\left(1 + \gamma \log_{10}\left(\frac{t}{t_0}\right)\right).$$

Here the creep is the only remaining motion towards the equilibrium after $t = t_0$ and γ describes the rate of the creep. This, similarly to thermal drift, causes a shearing and stretching of the image but with a decreasing amplitude across the scanning axes.

3 Structure of arachidic acid monolayers

For characterizing the structure of the arachidic acid monolayers (AAM) on HOPG we gathered STM images in which the structure of both the AAM and HOPG are visible. From those images we determined the intermolecular distance between two molecules of arachidic acid in their self-assembled lamellae structure as well as the size of its corresponding unit cell. The determination of the intermolecular distance is done by utilizing the presence of a Moiré pattern whilst comparing to a direct measurement.

A solution had to be prepared, in order to perform the in situ STM imaging. We dissolved commercially available arachidic acid in 1-phenyloctane in two steps to a concentration of around 116.4 mol $\cdot$ L^{-1}. After the tip has been withdrawn from our HOPG sample, we applied our solution onto the HOPG with a pipette. We ensured that a meniscus had formed, through the built-in lens of the NaioSTM air shield and afterwards approached our tip towards the HOPG surface. In order to study the structure of the AAM on HOPG, both structures have to be displayed in the same image. We adjusted the tip current threshold as well as the tip-sample voltage during the scanning procedure because we did not manage to find suitable parameters with which we can display both structures on the same set

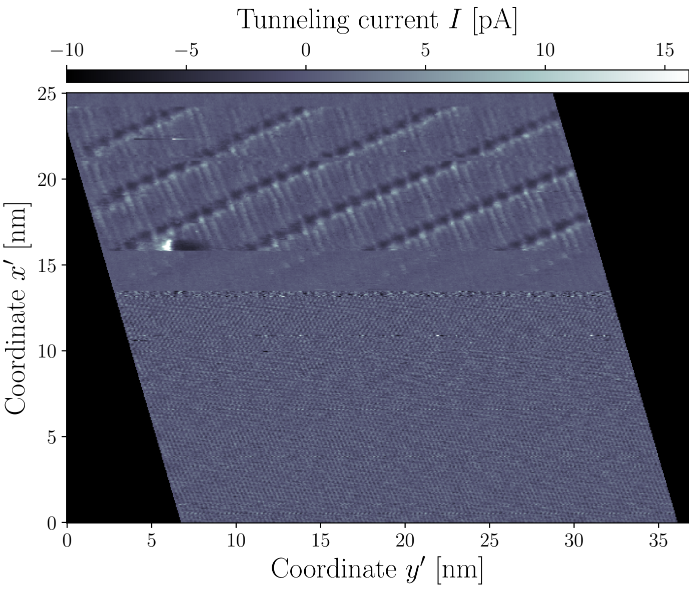

Figure 7 | Arachidic acid molecules self-assemble on the hexagonal graphite structure in rows of lamellae. Processed STM current-image where the tip current I is displayed in dependence of the drift-corrected coordinate pair (x', y'). The image partitioning is due to the adjustment of the tip current and tip-voltage during the scanning procedure which reveals the alignment of the AAM on HOPG.

of coordinates (x, y). This divided the image we obtained in figure 7 into two parts.

The lower portion of the image illustrates the structure of HOPG. We used it to perform the aforementioned post-processing workflow and to transform the whole image into the new coordinates (x', y'). An area of poor contrast and resolution forms a horizontal border between the two halves of the image, because we struggled with imaging the AAM directly after adjusting the operational parameters of the STM. We enhanced the contrast by applying voltage pulses of 4-10 V and width of <10 µs. A remnant of this approach is visible in figure 7 around $(x', y') \approx (16\text{ nm}, 7\text{ nm})$ where the pulse changed the local contrast yet enhanced the following signal-to-noise ratio and contrast. The remaining upper portion of figure 7 illustrates how the arachidic acid molecules assemble to form a flat monolayer. In this monolayer the molecules are packed in rows which are separated by the heads of the molecules (see figure 1). The heads appear in a darker shade in figure 7 because the carboxylic groups act as dimers as it was observed in a previous investigation [9]. We will refer to the direction parallel to each row, e.g. a vector connecting heads in one row, as the lamellae axis. Following the direction of the lamellae axis within one row, we find that the molecules arrange perpendicular to it with alternating the location of their head and tail. We also notice that within one row, each tails' brightness is not constant, but is spatially periodic. This periodicity in the brightness of the molecules' tails is a Moiré pattern.

We will exploit this pattern for the determination of the intermolecular distance d_{mol}, which is defined as the distance between each tail, measured parallel to the lamellae axis. The Moiré pattern is an interference pattern which forms because d_{mol} does *not* fulfill

$$n_{\text{mol}} \cdot d_{\text{mol}} = n_{\text{graph}} \cdot d_{\text{graph}} \tag{1}$$

for $n_{\text{mol}} = n_{\text{graph}} = 1$, where $n_{\text{mol}}, n_{\text{graph}} \in \mathbb{N}$ and the distance between parallel graphite axes $d_{\text{graph}} = 3/2 \cdot l \approx 2.132(2)$ Å. We denote the C-C bond length of the graphite lattice with $l = 1.421(1)$ Å [10] with the error assumed to be in the last significant reported digit. To determine d_{mol} from the current-images we have to find values of n_{mol} and n_{graph} for which the above equation is fulfilled. From the investigation of figure 7 we obtained the number of arachidic acid molecule tails that pack in one Moiré period $n_{\text{mol}} = 5$. Furthermore we follow the assumption of Thomas et al. [9] that $n_{\text{graph}} = 11$. With this we find the intermolecular distance in agreement with their findings to be $d_{\text{mol}} = 4.689(3)$ Å.

The intermolecular distance can also be obtained from a direct measurement in figure 7 because the carboxylic groups can be well distinguished from one another. The distance δ_{H} between two carboxylic groups measured in parallel to the lamellae axis, is double the intermolecular distance. By measuring distances s parallel to the lamellae axis that connect $k+1$ molecule heads, δ_{H} was determined by linear regression. We neglect local distortions in our processed image, with which we assume that

$$s(k) = \delta_{\text{H}} \cdot k \tag{2}$$

is a promising model for describing the dependence of s on k. Performing a fit ensures to reduce the influence of local stretches and skews as much as possible. Our data points were acquired with the image manipulation software GIMP by measuring the connection distances $\widetilde{s}(k)$ in units of pixels in the image and then converting them into real lengths using the anisotropic pixel pitches

$$\lambda_x = \frac{L_x}{p_x} \quad \text{and} \quad \lambda_y = \frac{L_y}{p_y}. \tag{3}$$

Where $L_{x,y}$ are the dimensions of the processed image in nanometers and $p_{x,y}$ the corresponding dimensions in units of pixels. When measuring each distance $\widetilde{s}_i(k_i)$ we also captured the corresponding angle φ_i with respect to the horizontal image edge. The conversion

Table 1 | Parameter and statistics resulting from the linear fit. Noted is the obtained distance δ_{H} that will be used for the determination of the intermolecular distance d_{mol} with the corresponding statistics which question the validity of the proposed model and uncertainties.

Parameter	Statistics		
δ_{H} [Å]	χ^2	χ^2_ν	$\mathcal{D}$
9.53(4)	32.8	3.28	0.80

from units of pixels into real lengths $s_i(k_i)$ follows with

$$s_i(k_i) = \tilde{s}_i(k_i)\sqrt{{\lambda_x}^2 \cos^2\varphi_i + {\lambda_y}^2 \sin^2\varphi_i}. \qquad (4)$$

The uncertainty in the connection distances $s_i(k_i)$ is introduced by L_x and L_y respectively. We assume a symmetrical error of $u_L = 3l$ in these these two physical quantities. The relative errors that result from the propagation in $s_i(k_i)$ are between 1% and 2% which stands in agreement with the other findings [11] where the relative error in distance measurements does not exceed 5%. This reinforces the validity of the assumption in u_L. Measurements corresponding to the same k_i were condensed by computing the mean and adding the standard error to u_L. We summarized the results and visualizations for the fit and its quality in table 1 and figure 8. A first inspection of the fit in figure 8a shows that roughly two thirds of our data points are consistent with the model within their error bars. The conversion from units of pixels into nanometers rendered our data to be heteroscedastic. We therefore conducted further investigations on the quality of the fit, by looking at the normalized residuals

$$R_i = \frac{1}{u_{s_i}}\big[s_i - s(k_i)\big]. \qquad (5)$$

In contrast to the visually acceptable agreement of the data and the model in figure 8a, the R_i in figure 8b reveal that only 72% of the data points exhibit $|R_i| \leq 2$, rather than 96%. Furthermore they follow a clearly non-random pattern for $k \leq 7$. This gives rise to the assumption that there is a systematic discrepancy which cannot be captured by our proposed model. The lag plot of the R_i in figure 8c also shows a slightly positive trend. This strengthens the assumption of systematic deviations because any non-random pattern in this kind of lag plot is an indicator for autocorrelations in the residuals. And finally we also computed the Durbin-Watson statistic [12]

$$\mathcal{D} = \frac{1}{\chi^2}\sum_{i=2}^{N}\big(R_i - R_{i-1}\big)^2$$

in tabel 1 which differs significantly from the expected value of $\mathcal{D} = 2$ for Gaussian residuals. We think that this systematic inconsistency is caused by the mechanism with which we obtained the values for the $s_i(k_i)$. The distance measurement between $k + 1$ carboxylic groups in figure 7 involved a rough determination of

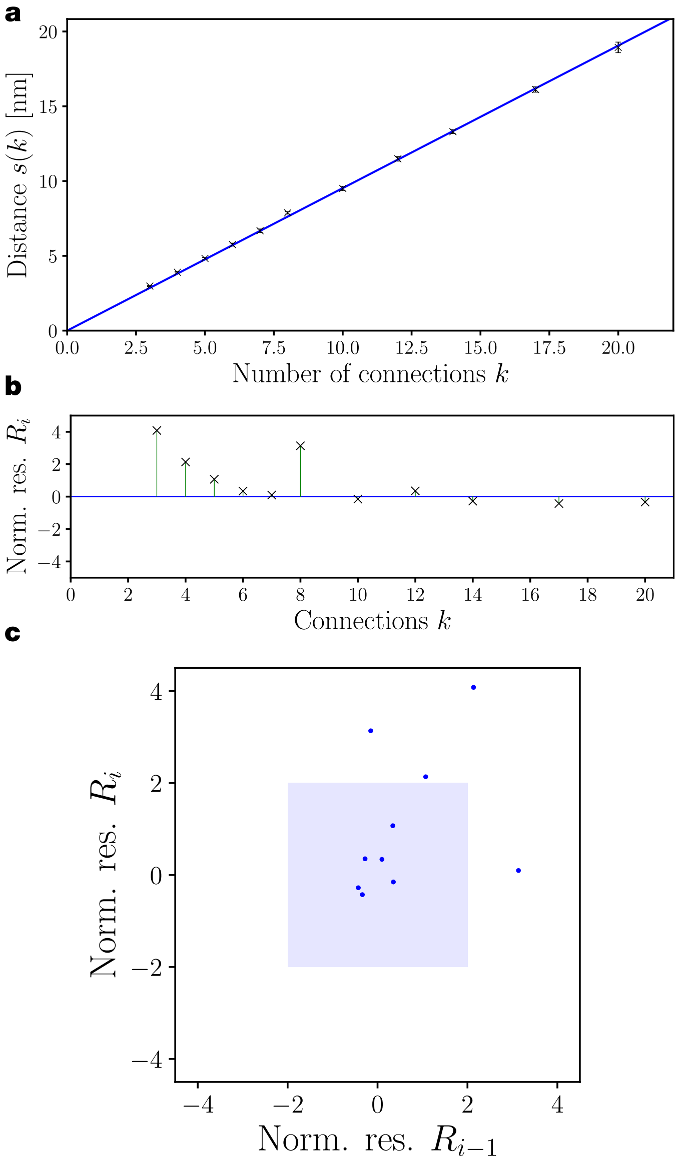

Figure 8 | Data visualization for the linear regression for the direct measurement of the intermolecular distance. a) Measured connection distances s_i against the number of connections k_i with the fit line. A first visual inspection yields acceptable agreement with the model as two thirds of the data are consistent within their error bar and the fit line. **b)** The normalized residuals R_i show that only 72% of the data points lie within *two* standard errors, indicating a poor fit. Furthermore they reveal a non-random deviation from the model. The green lines are a guide to the eye.**c)** Each R_i is plotted against the R_{i-1} which visualizes any non-random structure in the normalized residuals. For a good fit we expect 91% of the data to be contained inside the blue box.

two centers of molecule heads. Deviations in this rough determination will be more pronounced for a lower number of connections, which might explain why the $|R_i|$ in figure 8b get smaller for bigger k.

At last we also noted the goodness-of-fit parameters χ^2 and χ^2_ν in table 1 where $\chi^2_\nu = \chi^2/\nu$ with the number of degrees of freedom $\nu = 10$. For a reasonable fit we expect $\chi^2 \approx \nu$ or $\chi^2_\nu \approx 1$. We shall not reject the null hypothesis if χ^2 is within the bounds of two standard deviations $\sigma = \sqrt{2\nu}$ of its parent distribution i.e.

$$1.06 \leq \chi^2 \leq 18.94.$$

Our obtained χ^2 value falls out of this range by roughly 3σ. Because the probability distribution function of χ^2 has a skewed and non-trivial form for small ν we also wanted to look at the probability of obtaining such a χ^2 value with the cumulative probability function [12]

$$P(\chi^2, \nu) = \int_{\chi^2}^{\infty} X(\tilde{\chi}^2, \nu)\, \mathrm{d}\tilde{\chi}^2$$

where $X(\chi^2, \nu)$ is the probability density function of the χ^2 statistic. The probability of obtaining a statistic between the achieved χ^2 in table 1 and infinity is $P(32.8, 10) = 0.3 \cdot 10^{-3}$. The disagreement of model and data as it is proposed by the χ^2 statistic is either caused by a wrong estimation of the uncertainties in the $s_i(k_i)$ or by choosing the wrong model. As the origin of the uncertainties for STM operation are non-trivial, we think that a more detailed investigation of the working principle of the NaioSTM is needed to build an accurate description of the error in distance measurements. Regarding the chosen model, we can now say that the assumption of a linear dependence in the s_i on the k_i is questionable. We think that the influence of local distortions in the image by time dependent phenomena during the scanning procedure is too big for which they cannot be neglected. We also think that it is important to gather more data to invest the origin of the systematic discrepancies in the residuals as well.

Keeping this discussion in mind, we will compare our findings with the method utilizing the Moiré pattern. From the obtained value of δ_H we calculated the intermolecular distance $\widetilde{d}_\mathrm{mol}$ from the linear regression as $\widetilde{d}_\mathrm{mol} = 4.76(2)$ Å. This result lacks in precision and is less accurate as the findings that stand in agreement with the works of Thomas et al. [9]. Taking their error bars into account, both results are not consistent with each other. We think this deviation in $\widetilde{d}_\mathrm{mol}$ is due to the previously discussed systematic discrepancies in obtaining the $s_i(k_i)$. A well known [12] approach to obtaining an accurate and precise slope when performing a linear regression is to increase the precision of the measurements in the two limiting regimes. In our case for a low ($k \leq 5$) and high ($k \geq 15$) number of connections k. Looking back at the normalized residuals R_i in figure 8b we see that in the lower limiting regime an accurate determination of the connection distance $s_i(k_i)$ with respect to the model was not accomplished.

For a depiction of the unit cell with lattice vectors a and b see figure 4 in the the work of Thomas et al. [9]. The determination of the dimensions of the unit cell is straight forward since we computed $\delta_\mathrm{H} = a = 0.953(4)$ nm. Applying the same estimation of errors as previously discussed for the $s_i(k_i)$ we obtained $b = 3.06(5)$ nm by directly measuring b multiple times in figure 7 and taking the average over the data analogously to how we obtained the connection distances s_i. As we conducted the measurements for b we noted down the angles γ_i with respect to the horizontal image edge. In combination with the angles φ_i from equation (4) we computed the angle between the two lattice vectors a and b to be $\angle(a, b) \approx 82.21(4)$ °.

4 Structure of the HBC unit cell

Finally we also attempted to analyze the crystalline structure of the self-assembled monolayers of C_{12}-HBC. For this purpose we dissolved the organic compound in a solution of trichlorbenzene to an unknown concentration. We followed the previous methodology and applied the solution onto a freshly cleaved HOPG sample. Since the C_{12}-HBC molecules are significantly larger than those of arachidic acid, we had to increase the scanning range to 30 nm, which made it difficult to generate images where the underlying structure of the HOPG could be seen at a sufficient resolution. Nevertheless, we applied the methods described in the previous sections 3 and 2 for correcting linear distortions, we produced an image, in which one of the crystalline structures of the C_{12}-HBC monolayer can be observed. This enabled us to measure the primitive translation vectors of the unit cell. In order to reduce systematic errors we measured the lengths across multiple periods of the cell, as demonstrated in figure 9. We measured nine and four periods respectively.

Due to low resolution and sharpness of the image, we assume the position of the points, between the distances are measured, to have an uncertainty of $u_\mathrm{pos} = 2$ px in both the x- and y-directions. Since the lengths are determined as the absolute value of the two points' subtracted coordinates, this results in an error of $u_l = \sqrt{u_\mathrm{pos}}$, which is then also divided by the number of cells, over which the distance was measured.

The uncertainty in the angle between the lattice vectors, can also be determined from the uncertainty of the coordinates, as the angle φ between two vectors $\vec{a} = r_a(\cos(\varphi_a), \sin(\varphi_a))$ and $\vec{b} = r_b(\cos(\varphi_b), \sin(\varphi_b))$ is determined as $\varphi = |\varphi_a - \varphi_b|$. For each angle it holds that $\nabla\varphi_i = r_i^{-1}\mathrm{e}_\varphi$, where e_φ is the unit vector in transverse direction and since the uncertainty of the position was estimated to be the same in all directions, that results in an uncertainty for the angle of $u_\varphi = u_{\mathrm{pos}}\sqrt{r_a^{-2} + r_b^{-2}}$.

This approach to the uncertainties does not consider some of the biggest contributions to error in the measurement, like statistical factors such as noise, thermal fluctuations and nonlinear drifts, as we didn't conduct enough measurements to analyze them statistically. There is also the error in the affine transformation itself, stemming from the uncertainty of in the coordinates of the reciprocal lattice vectors, as doing the propagation of these errors analytically is fairly complicated and would require the parameters of the transformation used by SPIP, which we don't have access to.

The pixel-pitch in this image is nearly isotropic and amounts to about $\lambda \approx 0.0708$ nm. With this our results for the Bravais-lattice of one of the crystalline structures of $\mathrm{C_{12}}$-HBC can be seen in table 2, where $a = 9A$ and $b = 4B$.

Table 2 | Lattice constants of the monoclinic $\mathrm{C_{12}}$-HBC structure

lattice constant A	lattice constant B	angle φ
2.90(2) nm	4.78(5) nm	106.8(5)°

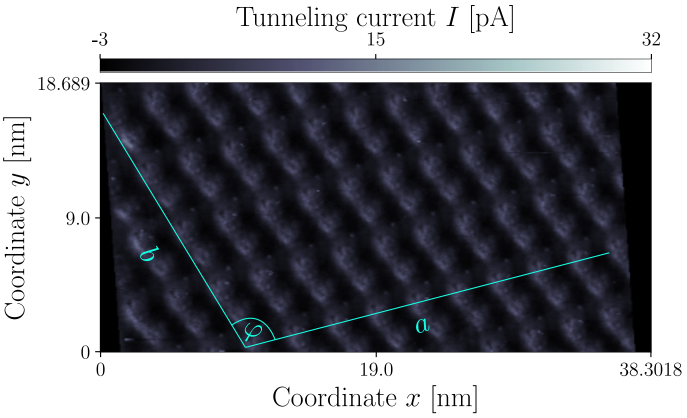

Figure 9 | Hexa-peri-hexabenzocoronene molecules aligning in a self-assembled monolayer on top of HOPG. Processed STM image of the tunneling current I in the approximated sample reference frame (x', y'). The methodology of the measurement for the unit cell lattice vectors across multiple cells is illustrated.

As stated before, the uncertainties here only represent those emerging from the measurement of distances and angles within an image and not the statistical and systematic errors inherent to the creation of the image itself. They are therefore almost certainly not representative of the true uncertainties.

The lattice we characterized here is not the only structure, in which $\mathrm{C_{12}}$-HBC assembles on top of HOPG, as can be seen in figure 10. The image showcases the boundary between two crystalline structures, which itself is unstable as the structure immediately around it changes over time, manifesting as distortions in the image.

Conclusion

While preparing and conducting the experiment we learned a lot about the modern ways of scanning tunneling microscopy and the image processing that is necessary for making the gathered data analyzable. We learned about the methods that are used by modern image processing tools to restore basic global distortions for which we understood the analytical background and their technical implementation. By utilizing HOPG as a calibration material in our setup we were able to show the advantages of this method over direct measurement techniques. We were able

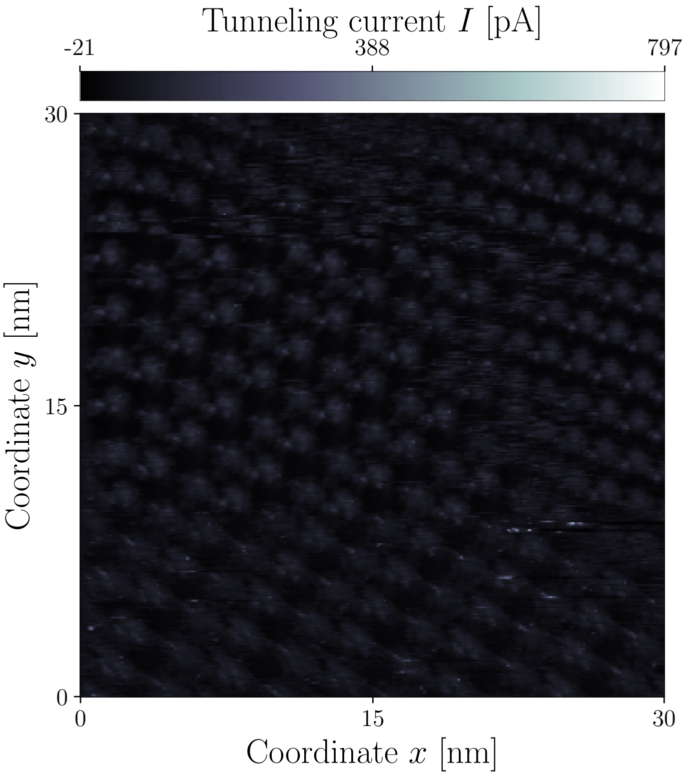

Figure 10 | The interface between two domains of different crystalline structures causes distortions in the image. Unprocessed image of the tunneling current across the HBC-sample to show that distance measurements involving the Moiré pattern is exceeding in precision and accuracy.

References

1. Binnig, G., Rohrer, H., Gerber, C. & Weibel, E. Surface Studies by Scanning Tunneling Microscopy. *Phys. Rev. Lett.* **49,** 57–61 (1982).
2. Hla, S. W. Atom-by-atom assembly. *Rep. Prog. Phys.* **77,** 056502 (2014).
3. Dujardin, G., Mayne, A., Robert, O., Rose, F., Joachim, C. & Tang, H. Vertical Manipulation of Individual Atoms by a Direct STM Tip-Surface Contact on Ge(111). *Phys. Rev. Lett.* **80,** 3085–3088 (1998).
4. Hla, S. W. & Rieder, K. H. STM Control of Chemical Reactions: Single molecule synthesis. *Annu. Rev. Phys. Chem.* **54,** 307–330 (2003).
5. Colton, R. J., Engel, A., Frommer, J. E., Gaub, H. E., Gewirth, A. A., Guckenberger, R., Rabe, J., Heckl, W. M. & Parkinson, B. *Procedures in Scanning Probe Microscopies* (John Wiley & Sons, 1998).
6. Rabe, J. P. & Buchholz, S. Direct observation of molecular structure and dynamics at the interface between a solid wall and an organic solution by scanning tunneling microscopy. *Phys. Rev. Lett.* **66,** 2096–2099 (16 1991).
7. Yothers, M. P., A. E., B. & L. A., B. Real-space post-processing correction of thermal drift and piezoelectric actuatornonlinearities in scanning tunneling microscope images. *American Institute of Physics* (2017).
8. Jung, H. & Gweon, D.-G. Creep characteristics of piezoelectric actuators. *Review of Scientific Instruments* **71,** 1896–1900 (Apr. 2000).
9. Thomas, L., Kühnle, A., Rode, S., Beginn, U. & Reichling, M. Monolayer Structure of Arachidic Acid on Graphite. *J. Phys. Chem. C* **114** (Oct. 2010).
10. Ergun, S. Structure of Graphite. *Nature Physical Science* **241,** 65–67. ISSN: 2058-1106 (1973).
11. Yurov, V. Y. & Klimov, A. N. Scanning tunneling microscope calibration and reconstruction of real image: Drift and slope elimination. *Review of Scientific Instruments* **65,** 1551–1557 (1994).
12. Hughes, I. & Hase, T. *Measurements and their Uncertainties: A Practical Guide to Modern Error Analysis* ISBN: 978-0-19-956632-7 (Oxford University Press Inc., 2010).